Collinear setup for delay control in two-color attosecond measurements

Journal of Physics: Photonics

OPEN ACCESS

RECEIVED
31 January 2020

REVISED
5 March 2020

ACCEPTED FOR PUBLICATION
23 March 2020

PUBLISHED
20 April 2020

PAPER

Collinear setup for delay control in two-color attosecond measurements

H Ahmadi[1,2], S Kellerer[1], D Ertel[1], M Moioli[1], M Reduzzi[2], P K Maroju[1], A Jäger[1], R N Shah[1], J Lutz[1], F Frassetto[3], L Poletto[3], F Bragheri[4], R Osellame[4], T Pfeifer[5], C D Schröter[5], R Moshammer[5] and G Sansone[1]

[1] Physikalisches Institut, Albert-Ludwigs-Universität Freiburg, 79106 Freiburg, Germany
[2] Dipartimento di Fisica, Politecnico, 20133 Milano, Italy
[3] Istituto di Fotonica e Nanotecnologie, CNR, 35131 Padova, Italy
[4] Istituto di Fotonica e Nanotecnologie, CNR, 20133 Milano, Italy
[5] Max–Planck-Institut für Kernphysik, 69117 Heidelberg, Germany

E-mail: hamed.ahmadi@physik.uni-freiburg.de **and** giuseppe.sansone@physik.uni-freiburg.de

Keywords: attosecond science, ultrashort laser, pump-probe spectroscopy

Abstract

We present a compact experimental setup for performing attosecond-pump-infrared-probe experiments with long-time delay stability. The robustness of the setup is demonstrated over a two-day acquisition time in two-photon photoionization of argon in the photon-energy range 17−33 eV. The propagation of the input infrared pulse, as driving pulse for the high-order harmonic generation process and for the generation of the sidebands of the main photoelectron peaks, through the main optical components is simulated and discussed. Our setup allows us to perform attosecond experiments with an overall stability of ± 40 as.

1. Introduction

Ultrashort laser sources are unique technological tools to resolve in time laser-matter dynamics on ultrafast timescales [1]. Nowadays, the highest temporal resolution of pump-probe experiments lies in the attosecond (1 as $= 10^{-18}$ s) domain and it is provided by the availability of ultrashort extreme ultraviolet (XUV) and x-ray pulses delivered either by high-order harmonic generation (HHG) in gases [2–4] or by Free-Electron Lasers [5, 6]. HHG-based XUV attosecond pulses are routinely used in time-resolved pump-probe spectroscopic techniques to initiate dynamics, which are then probed by a second pulse at a later time.

HHG sources operating up to MHz repetition rates have been demonstrated over the last years [7]. In combination with coincidence spectroscopy, based on Reaction Microscopes (ReMis) [8] or Cold Target Recoil Ion Momentum Spectroscopy (COLTRIMS) devices [9], HHG-based attosecond sources can be used for the investigation of molecular dynamics in the femtosecond [10] and attosecond [11] domain. In the case of small molecules, the complete reconstruction of the momenta distribution of the charged particles emitted in a photoionization/photodissociation process gives the possibility to separate the different dissociation channels triggered by the interaction with the pump pulse [11].

For the investigation of electronic dynamics occurring on the attosecond or sub-femtosecond time scale, the delay between pump and probe pulses needs to be controlled with a comparable precision. This requirement, combined with the long-acquisition times typical of coincidence measurements, represents a technical challenge for the implementation and development of attosecond coincidence spectroscopy. In many pump-probe measurements, a non-copropagating geometry, which requires an active stabilization setup [12–17], is used. This solution, however, adds complexity to the experimental apparatus. In this type of interferometer, an input beam is split into two beams propagating in different arms of the interferometer and the delay is controlled by changing the optical path length in one of the two arms. Such a setup requires both passive and active stabilization in order to minimize the temporal jitter due to the change in the optical path in each arm originating from airflow, thermal expansion of the mirrors, mechanical vibrations and beam pointing instability. By using active stabilization, in combination with beam pointing stabilization, a residual jitter of ~ 30 as has been obtained [18, 19].

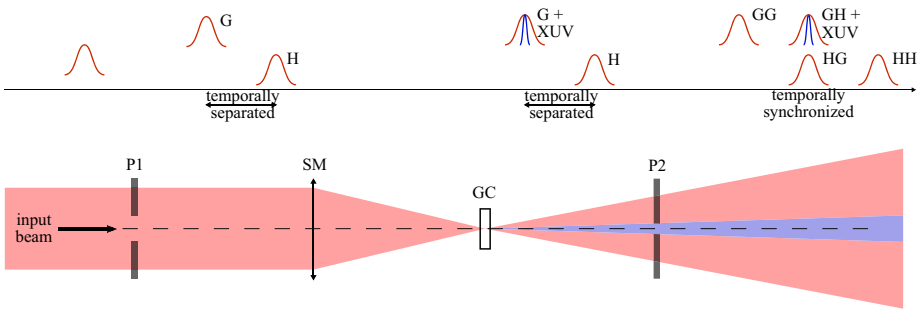

Figure 1. Schematic view of the delay line. The beam propagation through the main components of the setup is shown in the lower section. The input IR beam (red) with a Gaussian intensity profile, after passing the first plate P1, is focused by a spherical mirror (SM) into the HHG gas cell (GC), where XUV pulses are generated (blue). IR and XUV pulses then pass through the second plate P2. In the upper section, the beams created during the propagation are presented. The labels of the IR beams indicate the propagation through the glass (G) or the hole (H) of the plates. After traveling through the whole setup, four IR beams and an XUV beam should be considered. A temporal overlap is only possible for the beam GH/XUV and the beam HG. The time delay between the XUV and the HG pulse (IR dressing pulse) is controlled precisely by tilting P2 using a motorized rotation stage. The layout is adapted from [20].

Recently, a collinear geometry providing a time delay control of ~ 5 as with a stability of 7 as has been reported [20]. In this setup, a 5-mm-thick two-plate configuration (central and annular plates) is used to introduce a time delay between the two pulses [20]. The first plate with 5-mm diameter splits the input beam into two beams (central and annular beam), which are separated in time and space. Then the central pulse is used to generate the XUV radiation. The diameter of the first plate is chosen in such a way to ensure that the XUV light is generated by the central pulse. Then, the second plate exhibiting a central hole, is placed into the beam path to ensure the synchronization between the XUV and the infrared (IR) dressing pulses (annular pulse, which is going through the glass of the second plate). The time delay between the two pulses is controlled with a precision of about ~ 5 as by tilting the first plate (central plate). After the HHG medium, the central beam, which is copropagating and overlapping in time with XUV pulse, can be blocked by inserting an aluminum foil (typically 100-nm-thick) in the center of the second plate.

In our work, we present an alternative approach for a collinear delay setup with long-term delay stability. The experimental setup is based on two glass plates and it presents similarities, but also some important differences, with the experimental setup described in reference [20]. The propagation of the input IR beam through the main optical components is simulated and presented. We show the long-term delay stability of our experimental setup in a reconstruction of attosecond beating by interference of two-photon transitions (RABBITT) measurement, based on the characterization of the photoelectron spectra generated by the combination of an XUV attosecond pulse train and a synchronized IR pulse [2–4].

2. Two-plate setup configuration and delay calibration

Figure 1 shows schematically the arrangement of the two glass plates P1 and P2 with thickness $d \approx 1$ mm used in our setup. The propagation of the input IR beam (in red color) through the setup leads to four IR pulses and an XUV pulse (upper section). The labels (G, H, GG, GH, HG, and HH) of the IR pulses indicate the propagation through the glass (G) or hole (H) of one of the plates. In our setup, the hole diameter of P1 (d_1) is determined by the condition that only the pulse G generates XUV radiation (shown in blue color), while the harmonic generation by the IR beam H is negligible. Due to the lower divergence of the XUV light, the high-order harmonics pass with negligible losses through the hole of the plate P2 with diameter d_2. After P2, the temporal overlap with the XUV pulse is only possible for the pulse HG (GH), which propagates through the hole (glass) of the first plate and through the glass (hole) of the second one. The time delay between the XUV and the HG pulses (IR dressing pulse) is controlled precisely by tilting P2 using a motorized rotation stage. The time delay between the XUV and the GH pulses cannot be modified, but, as shown in the simulations, and as experimentally verified, the intensity of the GH pulse is negligible with respect to that of the HG pulse.

At normal incidence, the pulse GG, which propagates through two 1-mm-thick fused-silica glass plates, accumulates a group delay of ~ 4.89 picoseconds with respect to the XUV radiation and it does not contribute to the signal generated by the temporal overlap of the XUV and IR pulses. Also, the pulse HH, which passes through both holes, does not contribute to this signal because it arrives earlier than the XUV pulse.

The time or phase delay accumulated by the carrier-wave of the pulse with the central angular frequency ω_0 when the pulse propagates into a medium with thickness d and dispersion $n(\omega)$ can be defined as $\tau = \tau_p = \frac{\varphi(\omega_0)}{\omega_0} = \frac{n(\omega_0)\times d}{c}$, where $\varphi(\omega_0)$ is the phase of the central angular frequency ω_0. By tilting P2, we can control the time delay between the XUV and the IR dressing pulses, according to the equation [20]:

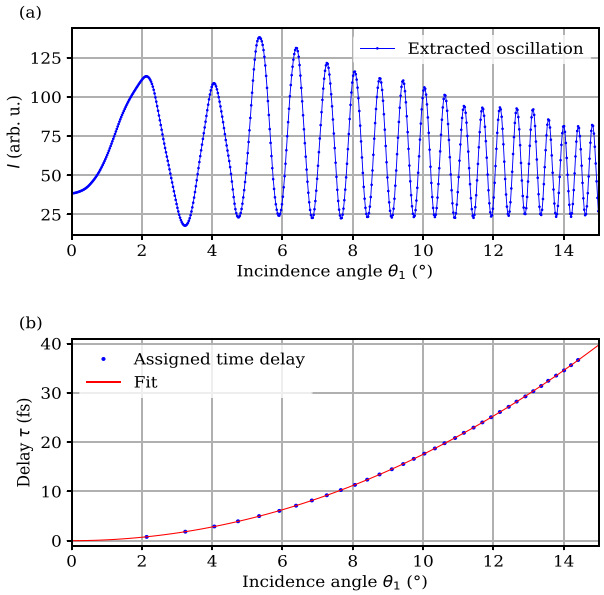

Figure 2. Calibration of the time delay τ introduced by tilting P2 using the He-Ne laser delivering continuous-wave radiation with wavelength 632.8 nm. (a) Extracted oscillation in intensity originating from the interference between the beam passing through the glass and hole of P2 dependent on the incidence angle of the beam with respect to P2 (θ_1). (b) Position of the interference maxima and minima extracted from panel (a) (blue dots) and fit of the experimental points according to equation (1) (red solid line).

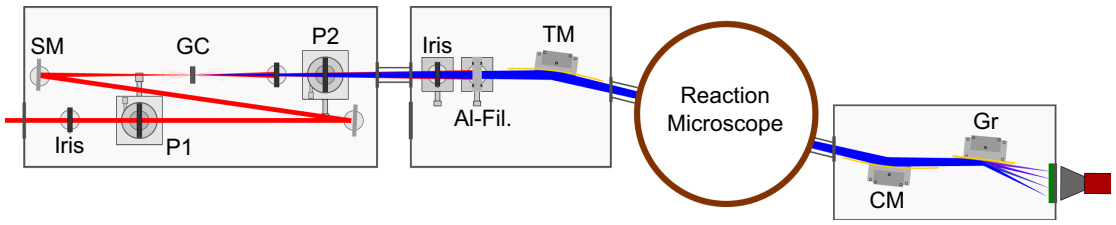

Figure 3. Experimental setup used in this work to perform a pump-probe experiment. P1: first delay plate; SM: spherical mirror; GC: gas cell; P2: second delay plate; TM: toroidal mirror; CM: cylindrical mirror; Gr: grating.

$$\tau = \frac{nd}{c}([\cos(\theta_2)]^{-1} - 1) + \frac{d}{c}[(\tan(\theta_1) - \tan(\theta_2)) \times \sin(\theta_1) - ([\cos(\theta_1)]^{-1} - 1)] \quad (1)$$

where n is the refractive index of the plate P2 at 800 nm, c is the speed of light, θ_1 is the incident angle on plate P2 and $\theta_2 = \arcsin(\sin(\theta_1)/n)$ is the refractive angle at the P2 interface. In order to calibrate the time delay τ as a function of the incidence angle θ_1 on the second plate, we measured the intensity evolution of the interference between the beams going through the hole and glass of the second plate P2 using a He-Ne laser operating at λ_{HeNe} =632.8 nm. From the measurement of the intensity variation (see figure 2(a)), the position of the maxima and minima was determined as a function of the incidence angle θ_1 as shown in figure 2(b). The experimental points were fitted (red solid line) using equation (1) in which the thickness of the plate d is used as a fitting parameter. The fit returns a value $d = 1.094 \pm 0.004$ mm, which is in agreement with the nominal thickness: $d_{\mathrm{nom}} = 1.0 \pm 0.1$ mm.

We should note that, in our configuration, the pulse broadening introduced by tilting the 1-mm-thick P2, corresponding to a time delay of 40 fs, is negligible.

3. Experimental setup

The two-color photoionization experiment was performed using a 10 kHz Ti:sapphire laser system providing 30-fs-long (FWHM) laser pulses centered at 800 nm with pulse energy of 1 mJ. This input pulse enters the attosecond beamline, which is shown in figure 3. The first glass plate P1, with central hole diameter d_1, splits the input radiation into two pulses (G and H), which are spatially separated and temporally delayed. The plates are fabricated by femtosecond laser irradiation followed by chemical etching; a machining technique that allows high control and precision in the shaping of structures fabricated in glass substrates [21]. The

procedure implemented for the fabrication of the plates ensures a very sharp boundary for the internal hole, thus ensuring an optimal focusing of different pulses in the experiment. Then, the collinear pulses are focused by a 25-cm-focal-length spherical mirror (SM) into a high-harmonic gas cell (GC) filled with argon. Using the iris placed before the plate P1, one can ensure that the XUV emission is generated only by the pulse G and that the pulse H does not significantly contribute to the harmonic spectrum. After the HHG cell, the second plate P2 with a central hole diameter d_2, centered with respect to the first plate, is used to synchronize the XUV and IR dressing pulses. While the XUV radiation passes through the hole of P2, the annular part of the pulse H, which is propagating through the second plate, overlaps in time with the XUV radiation (for plates of the same thickness). The delay between the two pulses can be then varied precisely by tilting P2. For the XUV-only measurements, an aluminum filter (Al-Fil) with a thickness of 100 nm is introduced into the beam propagation direction after the HHG cell in order to block the copropagating IR pulse. The XUV and IR dressing pulses are then refocused by a toroidal mirror (TM) into the interaction volume (IV) inside a 3D momentum imaging spectrometer (ReMi) leading to photoionization of argon at an ion count rate of less than one per XUV pulse. The TM creates an image of the HHG-source point in the focal region of the ReMi with unitary magnification using input and output arm length of 0.9 m. The ions and electrons released at the center of the spectrometer are guided using a homogeneous electric field ($E \sim$ 313 V m^{-1}) and a weak magnetic field ($B \sim 9.4$ Gauss) towards time- and position-sensitive detectors located at the opposite ends of the spectrometer [22]. The longitudinal and transverse momentum resolution for a typical 4.23 eV photoelectron ($p_r = 0.25$ and $p_z = 0.5$ a.u.) is $\delta p_z \sim 0.03$ a.u. and $\delta p_r \sim 0.02$ a.u., respectively. Finally, the XUV pulse is directed to an XUV spectrometer composed of a cylindrical mirror (CM) and a concave grating (Gr), leading to dispersion of the spectral components in the focal plane, where an MCP coupled to a phosphor screen is placed. The signal at the back of the phosphor screen is monitored by a CCD camera.

We should note that our setup is different in a few aspects from the previous work in Zaïr's group [20]. Instead of using a central and an annular plate, we use two 1-mm-thick glass plates with different central hole sizes (typically $d_1 = 2.5; 3.0$ mm and $d_2 = 0.5; 1.0$ mm holes for the first and second plate, respectively). In our setup, the annular pulse G is responsible for the generation of the XUV radiation, while the pulse HG provides the IR dressing one. In this way, the dressing pulse propagates closer to the optical axis of the experimental setup, improving its focal properties, which are less sensitive to imperfections on the edges of the optical elements (in particular of the toroidal mirror surfaces used to refocus the XUV and IR pulses). Using our approach, in principle, it is not necessary to use an aluminum filter since there is no significant fraction of the IR pulse GH, which is transmitted through the hole of the second plate and overlaps in time with the XUV radiation.

4. Simulation of beam propagation

A few important aspects need to be considered in the design and dimensioning of the optical components of our setup. The first important point is to make sure that the XUV radiation (pump pulse in our setup) is only generated by the annular pulse G. This requires that the intensity of the pulse G must be significantly higher than that of the pulse H at the focus where the gas cell is placed. The intensity of the IR dressing pulse (HG) is the second important point to be considered. We should make sure that the intensity of the pulse HG is much larger than that of the pulse GH, which also temporally overlaps with the XUV radiation. If this condition is not fulfilled, interference effects due to the temporal overlaps of the two IR pulses would be visible. In this section, we aim at addressing and discussing these points by simulating the propagation of the input IR pulse through the experimental setup. We numerically solve the Huygens-Fresnel-Kirchhoff integral in the Fresnel approximation (assuming parabolic wavefronts) combined with the ABCD matrices formalism [23]. For simplicity, the focusing optics are described by lenses, which do not change the focusing properties, even if in the real setup focusing mirrors are used. The components are aligned in such a way that the foci of the lenses and the centers of the plate's holes lie on the optical axis, where the initial Gaussian beam has its maximum in intensity. The propagation of the input beam is considered here in paraxial approximation in which the propagating beam is assumed to make only a small angle to the optical axis of the system and lies close to it [24]. The electric field $\tilde{u}(r)$ on the output plane z originating from the field $\tilde{u}(r')$ on the input plane z_1 can be expressed in cylindrical coordinates as [24]:

$$\tilde{u}(r) = \frac{ik}{B} \exp\left(-\frac{ik}{2B} D r^2\right) \times \int_{\tilde{R}} \tilde{u}(r') r' J_0\left(\frac{k}{B} r' r\right) \exp\left(-\frac{ik}{2B} A r'^2\right) \mathrm{d}r', \quad r' \in \tilde{R}, \tag{2}$$

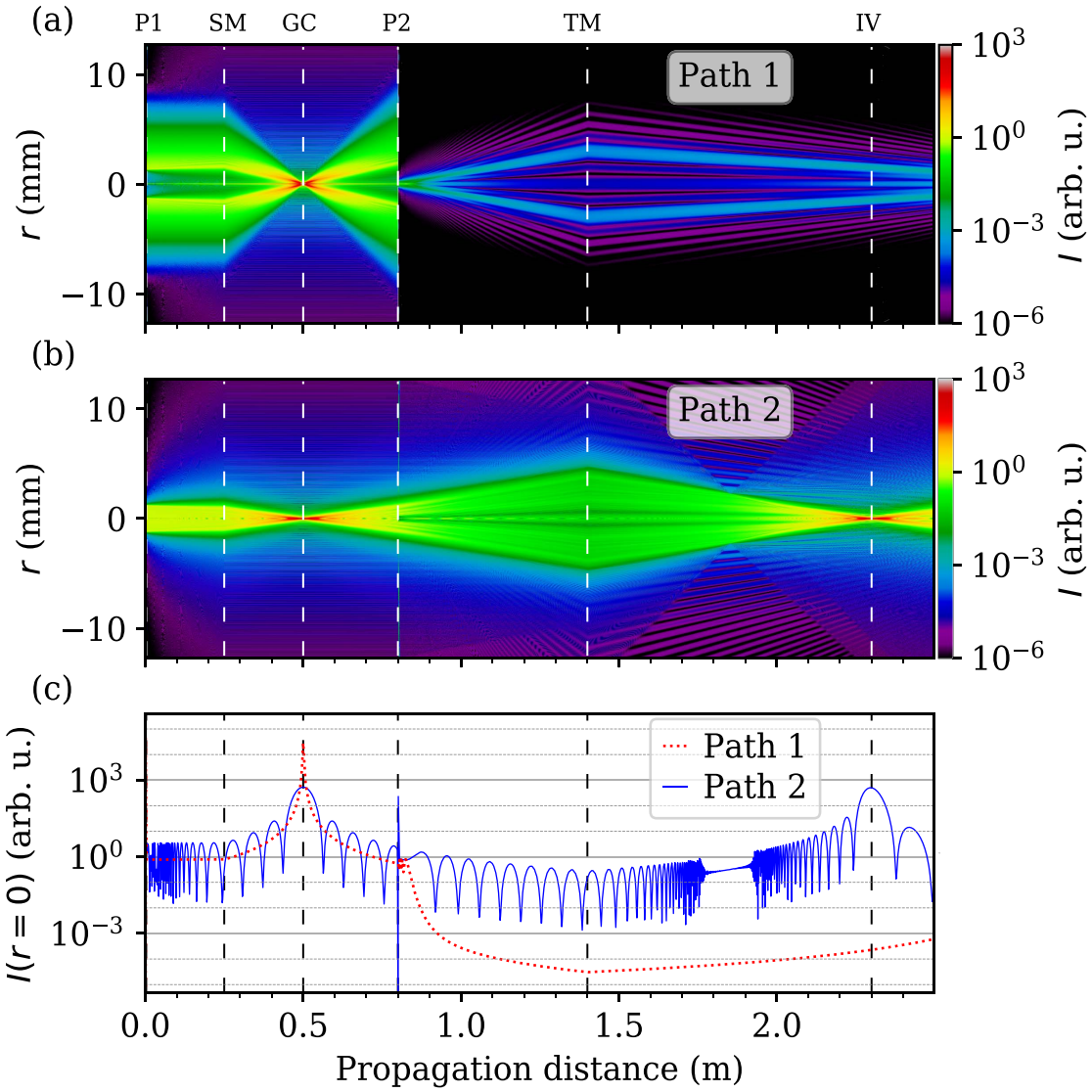

Figure 4. Simulation of propagation of the input IR beam through the experimental optical setup. (a) propagation of the input beam going through the glass of the first plate and the hole of the second plate (beams G and GH) which is referred to Path 1. (b) propagation of the input beam passing through the hole of the first plate and glass of the second plate (beams H and HG) which is referred to Path 2. The position of the first plate P1, spherical mirror (SM), gas cell (GC), second plate P2, toroidal mirror (TM) and interaction volume (IV) are indicated with dashed vertical lines. (c) Corresponding intensity of Path 1 (red dotted line) and Path 2 (blue solid line) calculated at $r = 0$.

where k is the wavenumber, J_0 is the Bessel function of zero order, $\tilde{R}$ is the integration interval ($\tilde{R} = [0, R]$ for the central beam and $\tilde{R} = (R, \infty)$ for the annular beam where R is the radius of the hole). The quantities A, B and D depend on the optical system (such as free propagation regions and focusing optics) present between the z and z_1 planes. The first plate P1 splits the input IR pulse into the two pulses G and H, which are delayed in time with respect to each other. As a result, the two pulses can be treated separately in the simulation. Due to diffraction effects, the shape and intensity distribution of the pulses will change during the propagation. For the central pulse, the input Gaussian beam is multiplied by a step function, which is 1 if $r < R$ and zero otherwise. For the annular pulse, the values of the step function are inverted (0 if $r < R$, 1 otherwise). For simplicity, we consider a monochromatic wave with wavelength $\lambda = 800$ nm, which is the central wavelength of the laser pulse used in the experiment. We should note that the first propagation steps directly after each plate shown in figure 4 are not physical because of the finite sampling in the radial direction. The numerical results can be improved by increasing the number of sample points in the radial direction but at the expenses of higher computation times.

We have performed the simulation for two paths referred to Path 1 (corresponding to the pulse GH) and Path 2 (corresponding to the pulse HG). Figure 4 presents the intensity in logarithmic color scale of the pulses GH (a) and HG (b), respectively. The input pulse has a Gaussian intensity profile ($I_{\max} = 1$ a.u.), a beam waist of $w_0 = 3.5$ mm at a wavelength $\lambda = 800$ nm, corresponding to the experimental parameters. The hole diameters d_1 and d_2 are set to 2.5 and 0.5 mm, respectively. For each of these positions, the

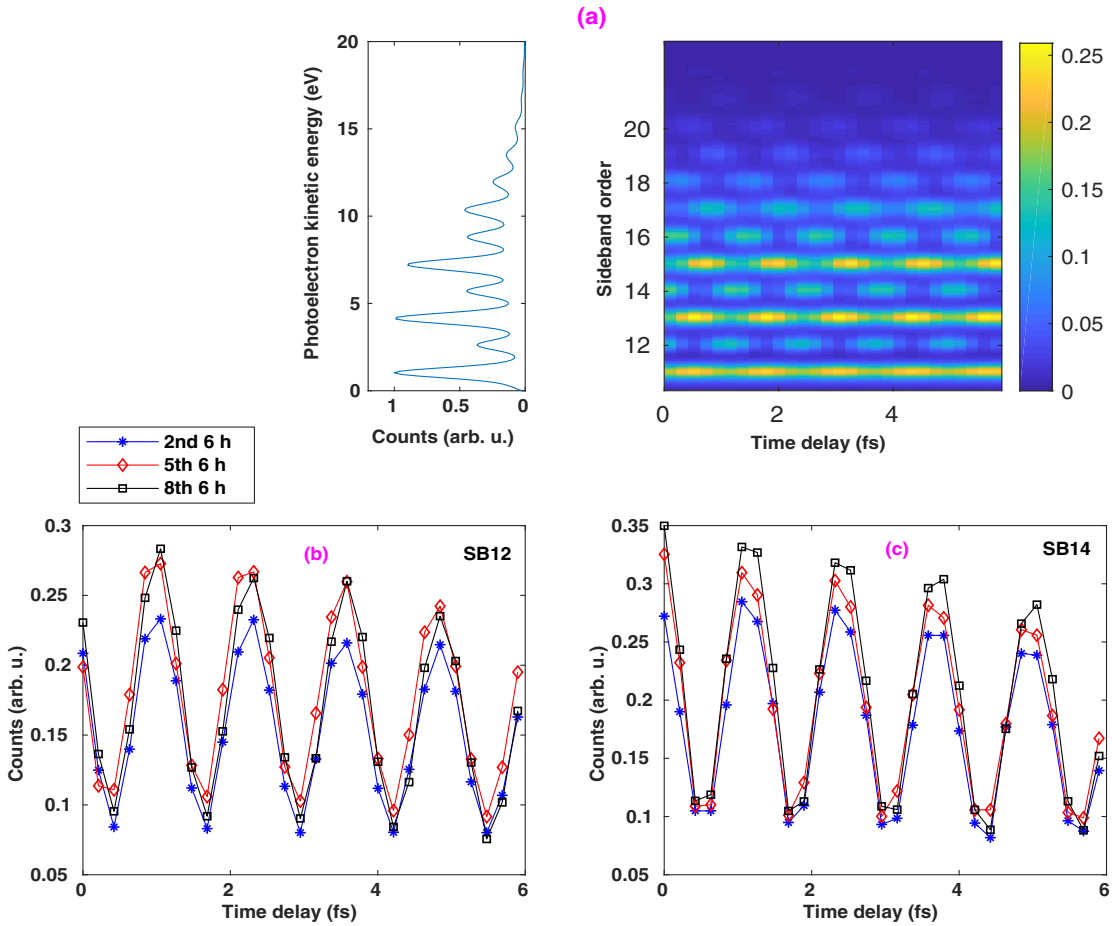

Figure 5. RABBITT trace measured in argon for a two-day acquisition time together with the corresponding delay-integrated photoelectron spectrum (a). The oscillations of SB12 (b) and SB14 (c) for three time intervals of the acquisition (second 6 h (blue line with asterisk), fifth 6 h (red solid line with diamond) and eighth 6 h (black solid line with square)). The sideband signal is calculated in a window of 0.75 eV around the peak of the sideband position.

simulation was performed for $r \in [0, 12.7\ \text{mm}]$, with 48 640 steps, i.e. $\Delta r \approx 2.6 \times 10^{-4}$ mm. For a better visualization, the values were mirrored afterward to cover the region of $r \in [-12.7\ \text{mm}, 12.7\ \text{mm}]$.

The propagation here starts directly at the first plate, where the pulses G and H are separated in time. After free propagation of 0.25 m, the beam is focused by a 25-cm-focal-length spherical mirror (SM). After diverging over a distance of 0.3 m, the beam passes the second plate. Afterward, the pulse is propagating towards the second focusing optic (TM), which is placed at 1.4 m. After the second plate, Path 1 shows a few peaks along the radial direction which depends strongly on the chosen hole diameters. In contrast to Path 2, for the input values chosen here, the remaining IR part of the beam is not focused into the interaction region, which is located at a position of 2.3 m. The small hole of the second plate defines the source point of the beam GH; the distance of this point to the toroidal mirror is smaller than its input arm length (0.9 m). As a consequence, the beam is focused at a larger distance than the output arm length after the toroidal mirror. Therefore, for Path 1, the beam GH is not focused in the interaction region of the ReMi. In order to see the relative intensity achievable in our setup for the Path 1 and 2, we present in figure 4(c) the intensity evolution of the two pulses along the optical axis (calculated at $r = 0$). One can easily observe that the intensity reached in the focus corresponding to the gas cell (propagation distance of 0.5 m) is a few orders of magnitude higher for pulse G with respect to the one of pulse H (about two orders of magnitude). This observation ensures that the generation of XUV radiation is due to the annular part of the input pulse. One can also observe that at the second focal point located at a propagation distance of 2.3 m and corresponding to the interaction point in the ReMi, the intensity of the IR pulse HG (which is IR dressing pulse in our setup) is much higher (about six orders of magnitude) than the pulse GH.

5. Long-term stability

In order to demonstrate the long-term stability of our experimental setup, we performed a RABBITT (reconstruction of attosecond beating by interference of two-photon transitions) measurement, which is

based on the single-photon ionization by a train of attosecond pulses and the subsequent absorption and/or emission of an IR photon [2]. Photoelectron kinetic energy is recorded as a function of time delay τ between the XUV-pump and IR-probe pulses. The XUV pulse consists of odd multiples of the fundamental frequency ω_{IR} of the IR probing laser and, therefore, the photoelectron spectrum shows discrete peaks corresponding to the absorption of a single XUV photon with energy higher than the ionization potential of the atom (argon in this case). The subsequent absorption or emission of one IR photon leads to appearance of the sidebands (SB) in between the harmonics. For each SB order $2q$, two indistinguishable excitation pathways are involved: (1) absorption of one photon from harmonic $2q-1$ followed by the absorption of an additional IR photon, and (2) absorption of one photon from harmonic $2q+1$ and subsequent emission of an IR photon. Because of two-quantum-path interference, the SB intensity shows an oscillation by varying the time delay (τ): $A_{SB} \propto \cos(2\omega_{IR}\tau - \phi_{XUV} - \phi_{atom})$. Here, ϕ_{XUV} is related to the phase difference between consecutive harmonics, while ϕ_{atom} is the phase due to the two-color photoionization process.

Figure 5(a) presents the RABBITT trace measured in argon for an acquisition time of 54 hours (right panel) and its corresponding total photoelectron spectrum averaged over the entire delay range (left panel). We have used 29 delay steps with steps of 200 as corresponding to a delay range of 5.8 fs between the two pulses. The XUV and IR dressing pulse intensities are estimated to be $I_{XUV} = 1.9 \times 10^{10}$ W cm^{-2} and $I_{IR} = 10^{12}$ W cm^{-2}, respectively. Figures 5(b) and (c) show the intensity of SB12 and SB14 as a function of the XUV-IR delay for three different time intervals, each corresponding to 6 hours of acquisition time. The sideband signal is obtained by integrating in an energy window of 0.75 eV around the position of the sideband peak. The data acquired during the 54 h acquisition time are divided into 9 data sets. For each data set, the oscillation phase for different sidebands is retrieved by fitting a cosine function into each oscillation. Then, for each sideband, the standard deviation in phase retrieval of 9 data sets is calculated. The resulting standard deviation in phase for SB12, SB14 and SB16 was ~ 0.19 radian which corresponds to an error in time delay of $\sim \pm 40$ as which we consider as stability of our delay-line setup. In the work of Isinger *et al* [25], one can find more detailed information about different parameters affecting the accuracy and the precision of the RABBITT technique in retrieving the photoionization time delay.

6. Conclusion

In this work, we have presented an ultrastable setup for performing pump-probe measurements using attosecond and IR laser pulses. The collinear setup consists of two 1-mm-thick fused-silica glass plates with different diameters of the central holes. The experimental setup does not require any active stabilization and allows us to induce very small delay steps (even below 5 as).

In order to demonstrate the long-term stability of our setup, the photoelectron spectrum from two-color photoionization of argon using a ReMi was recorded over 54 hours of acquisition for time delays in the range $0 \leq \tau \leq 5.8$ fs between the XUV and IR dressing pulses. Comparing the oscillation phase of three sidebands SB12, SB14 and SB16 for 9 data sets of 6 h intervals confirms a stability of ± 40 as for the delay-line setup over 54 h acquisition time. The delay unit will be used for the acquisition of photoelectron/photoion coincidence spectra of small molecules and in gas mixtures of atoms and molecules. Using our approach it should be possible to characterize channel-resolved attosecond time delays on the order of a few tens of attoseconds.

Acknowledgment

We acknowledge the contribution of Dr I Breunig and Y Minet (Institut für Mikrosystemtechnik-IMTEK, Albert-Ludwigs-Universität Freiburg) in the preparation of the drilled plates used in the delay-unit. This project has received funding from the European Union's Horizon 2020 research and innovation program under the Marie Sklodowska-Curie grant agreement no. ~ 641789 MEDEA, the Italian Ministry of Research (Project FIRB No. RBID08CRXK) and the Deutsche Forschungsgemeinschaft (DFG) (IRTG CoCo (2079), INST 39/1079 (High-Repetition-Rate Attosecond Source for Coincidence Spectroscopy), QUTIF SA 3470/2). Funding from the Bundesministerium für Bildung und Forschung (Project 05K19VF1) is gratefully acknowledged.

ORCID iD

H Ahmadi https://orcid.org/0000-0003-1610-5811

References

[1] Krausz F and Ivanov M 2009 *Rev. Mod. Phys.* **81** 163–234

[2] Paul P, Toma E, Breger P, Mullot G and Augé F 2001 *Science* **292** 1689
[3] Li J *et al* 2017 *Nat. Commun.* **8** 186
[4] Gaumnitz T, Jain A, Pertot Y, Huppert M, Jordan I, Ardana-Lamas F and Wörner H J 2017 *Opt. Express* **25** 27506–18
[5] Duris J *et al et al* 2020 *Nat. Photon.* **14** 30–6
[6] Maroju P K *et al* 2020 *Nature* **578** 386–91
[7] Hädrich S, Klenke A, Rothhardt J, Krebs M, Hoffmann A, Pronin O, Pervak V, Limpert J and Tünnermann A 2014 *Nat. Photon.* **8** 779
[8] Ullrich J, Moshammer R, Dorn A, Dörner R, Schmidt L P H and Schmidt-Böcking H 2003 *Rep. Progress Phys.* **66** 1463–545
[9] Dörner R, Mergel V, Jagutzki O, Spielberger L, Ullrich J, Moshammer R and Schmidt-Böcking H 2000 *Phys. Rep.* **330** 95–192
[10] Sandhu A S *et al* 2008 *Science* **322** 1081–5
[11] Vos J, Cattaneo L, Patchkovskii S, Zimmermann T, Cirelli C, Lucchini M, Kheifets A, Landsman A S and Keller U 2018 *Science* **360** 1326–30
[12] Müller H G 2002 *Appl. Phys.* B **74** s17–s21
[13] Wang H, Chini M, Khan S D, Chen S, Gilbertson S, Feng X, Mashiko H and Chang Z 2009 *J. Phys. B: At. Mol. Opt. Phys.* **42** 134007
[14] Chini M, Wang H, Khan S D, Chen S and Chang Z 2009 *Appl. Phys. Lett.* **94** 161112
[15] Chini M, Mashiko H, Wang H, Chen S, Yun C, Scott S, Gilbertson S and Chang Z 2009 *Opt. Express* **17** 21459–64
[16] Frank F *et al* 2012 *Rev. Sci. Instrum.* **83** 52
[17] Böttcher F, Manschwetus B, Rottke H, Zhavoronkov N, Ansari Z and Sandner W 2008 *Appl. Phys.* B **91** 287–93
[18] Huppert M, Jordan I and Wörner H J 2015 *Rev. Sci. Instrum.* **86** 123106
[19] Huppert M, Jordan I, Baykusheva D, Von Conta A and Wörner H J 2016 *Phys. Rev. Lett.* **117** 093001
[20] Zaïr A, Mével E, Cormier E and Constant E 2018 *J. Opt. Soc. Am.* B **35** A110–A115
[21] Vishnubhatla K C, Bellini N, Ramponi R, Cerullo G and Osellame R 2009 *Opt. Express* **17** 8685–95
[22] Ullrich J, Moshammer R, Dorn A, Dörner R, Schmidt L P H and Schmidt-Böcking H 2003 *Rep. Progress Phys.* **66** 1463
[23] Svelto O 2010 *Principles of Lasers Springer* (New York: Springer)
[24] Lin C D, Jin C, Le A T and Wei H 2018 *Attosecond and Strong-Field Physics: Principles and Applications* (Cambridge: Cambridge University Press)
[25] Isinger M, Busto D, Mikaelsson S, Zhong S, Guo C, Salières P, Arnold C, L'Huillier A and Gisselbrecht M 2019 *Phil. Trans. R. Soc.* A **377** 20170475